Defect and Diffusion Forum
ISSN: 1662-9507, Vol. 451, pp 111-123
doi:10.4028/p-FW1Rb0

Submitted: 2026-01-19
Revised: 2026-02-19
Accepted: 2026-02-25
Online: 2026-04-17

From Deposition Sequence to Mechanical Response: A Macroscale Process Simulation of Material Extrusion

DI NARDO Mario Emanuele[1,a*], RUSSO Pietro[2,b] and CARLONE Pierpaolo[1,c]

[1]Department of Industrial Engineering, University of Salerno, 132 Via Giovanni Paolo II, 84084 Fisciano (SA), Italy

[2]Institute of Polymers, Composites and Biomaterials, National Research Council, Via Campi Flegrei 34, 80078 Pozzuoli, Italy

[a]mdinardo@unisa.it, [b]pietro.russo@ipcb.cnr.it, [c]pcarlone@unisa.it

Keywords: Additive Manufacturing, MEX, FFF, Process Simulation, FEM, Thermomechanical Analysis

Abstract. The deposition sequence and the resulting thermal history govern the development of distortions and residual stresses in components made by material extrusion, ultimately affecting their structural performance. This work presents a process-aware thermomechanical simulation framework that reproduces the actual deposition directly from the G-Code. The nozzle trajectory is processed to reconstruct the bead order and timing and to automatically generate a voxel-based finite element mesh suitable for progressive activation. A transient thermal analysis is then performed with incremental element activation, while the thermal effect of extrusion is prescribed through a temperature predefined field applied to the newly activated elements, together with convective-radiative heat losses to the environment. The resulting temperature history is subsequently transferred as a time-dependent temperature field to a quasi-static mechanical analysis to predict residual distortions and stresses after cooling. Finally, a linear elastic virtual tensile test is carried out on the final, deformed configuration, accounting for the residual stress state. The framework is applied to PLA ASTM D638 specimens manufactured at different extrusion temperatures and validated against experimental tests, showing that extrusion temperature governs thermal gradients, residual stress distributions and the resulting macroscopic elastic response.

Introduction

Material extrusion (MEX), referred to as fused filament fabrication (FFF) when the raw material is in filament form, is one of the most widely used additive manufacturing (AM) processes for thermoplastic polymers due to its ability to produce complex geometries with low mass and good mechanical performance [1]. However, the quality and mechanical response of the components are highly dependent on the process. In fact, strand by strand deposition imposes a highly variable local thermal history which can introduce filling criticalities and reduce adhesion between layers. Furthermore, the nozzle path determines the internal structure, inducing anisotropy and therefore variable stiffness depending on the orientation of the strands [2]. In other words, the thermal history induced by the process, governed by the nozzle trajectory and temperature parameters, regulates both the consolidation between strands and the overall response of the component [3]. On the microscale, the temperature of adjacent beads controls the diffusion of the polymer at the interface and therefore the quality of the adhesion, with direct effects on the porosity [4]. On the macroscale the thermal gradients associated with the cooling of each individual bead induce residual stresses and distortions that can compromise dimensional accuracy and alter the measured mechanical response [5,6]. More generally, linking process conditions to transport phenomena and the onset of process induced defects is a recurring theme across additive manufacturing and, more broadly, across many manufacturing processes [7,8]. Given that, in order to control the effect of process parameters on mechanical response, a predictive approach is needed that can reproduce the actual deposition sequence, so as to establish a quantitative link between the nozzle path, thermal history and final component behaviour. In this context, finite element method (FEM) process simulations provide a solid framework for connecting process and performance. Early work placed strong emphasis on validated thermal histories. Roy et al. proposed a transient thermal framework in which deposition follows the programmed path and experimentally validated the predicted temperature evolution using non-contact infrared sensing on the part, showing that the model can capture the spatiotemporal thermal profile during deposition and subsequent cooling [5]. On this basis, subsequent studies have extended the approach to sequential thermomechanical workflows, transferring the calculated temperature as a predefined field to a subsequent mechanical analysis to estimate residual distortions and stresses. Trofimov et al. presented a model with progressive activation along the trajectory and experimental validation of both the thermal distribution and the final distortion [6]. However, it remains challenging to faithfully reproduce the gradients and time scales of the process at sustainable computational costs. In fact, capturing localized gradients requires fine meshes and short time increments, which can make parametric analyses prohibitive. Ramos et al. explicitly addressed this point by proposing efficiency measures, such as hybrid activation and adaptive coarsening, while maintaining model validation [9]. Generally, to make process simulations feasible in an FEM environment, one of the most used techniques is the progressive activation of elements, so that geometry and heat distribution follow the tool path. In Abaqus, these features are available through dedicated tools, including the use of event series to describe trajectories and activation times of elements and deposition [10]. The bottleneck often remains the translation of slicer data and, in fact, the G-Code part program into FEM models inputs. Discretization compatible with progressive activation and a sufficiently accurate but computationally efficient description of events are required. Generally, this need for a robust workflow that converts CAD or process programs into executable toolpaths and, subsequently, into simulation ready inputs is not unique to MEX, but emerges across many AM applications whenever geometric descriptions must be translated into consistent machine trajectories and then reprocessed into analysis data [11,12]. Beyond this data-translation step, achieving repeatable outcomes often depends on system level coordination of process timing, thermal history, and hardware functionalities, since these aspects jointly define the effective boundary conditions experienced by the material [13]. In recent years, methodologies aimed at automatic conversion have been introduced that directly integrate the path description into the structural analysis and optimization workflow [14,15,16]. However, despite these advances, robust and generalizable end-to-end workflows that simultaneously preserves sequence, timing, and deposited volume remains an open goal and, for many applications, a still highly manual step. As described in Figure 1, this work therefore proposes a sequential thermomechanical chain guided directly by the deposition sequence, aimed at establishing a quantitative macroscale link between nozzle trajectory, thermal history, and final linear elastic response. Starting from the standard slicer outputs, the G-Code is processed through a python script to reconstruct the nozzle coordinates and deposition timing, while the geometry constrains and controls the activated volume. The inputs are converted into FEM input files, a series of events with process activation and timing and a voxel-based mesh compatible with progressive deposition, with voxel size consistent with the scale of the deposited bead. A transient thermal analysis is then performed to obtain the thermal history $T(x,t)$ during deposition. This is then imported as a time-dependent predefined field into a quasi-static mechanical analysis to estimate residual stresses $\sigma(x,t)$. Finally, virtual displacement control tests are performed on the deposited and cooled, and therefore potentially distorted mesh to obtain the tensile response in the linear elastic regime, including the effect of the residual stress state induced by the process. In this work, the approach is applied to PLA samples with 0/90° infill and different nozzle temperatures, adopting temperature-dependent material properties to represent the evolution of stiffness and thermal deformation during manufacturing. Validation is performed by tensile testing according to ASTM D638 [17], comparing the response in the linear elastic regime. Overall, this work aims to provide a practical and computationally manageable path from the deposition sequence to mechanical performance, supporting the selection of process parameters.

Methodology

Deposition sequence processing

Starting from the component geometry provided in Standard Triangle Language (STL) format and from the nozzle path encoded in the G-Code, a Python conversion tool generates two FEM inputs, an event series describing the nozzle trajectory in time with a binary deposition state and a structured voxel mesh suitable for element progressive activation according to the nozzle coordinates. The STL geometry is used exclusively as a volume constraint to retain only voxels that lie inside the nominal part volume. As shown in Figure 1, at first the G-Code is parsed sequentially, in order to translate the part program language into a dataset with process time associated with the cartesian coordinates assumed by the nozzle when depositing. For simplicity in this application, only linear motion commands G0/G1 are interpreted as nozzle motion. The nozzle coordinates x, y, z are treated as modal, meaning that values not specified in a line retain the most recent value. The feedrate F is also treated as modal and interpreted in mm/min, consistent with common G-Code conventions. For clarity, F is the commanded toolpath feedrate that sets the nozzle translational speed along each G0/G1 segment, whereas E is the commanded extruder axis coordinate that specifies the amount of filament to be pushed through the nozzle. While F controls the kinematics, changes in E quantify material delivery. Given that, material extrusion is tracked through the E axis, supporting both absolute M82 and relative M83 modes.

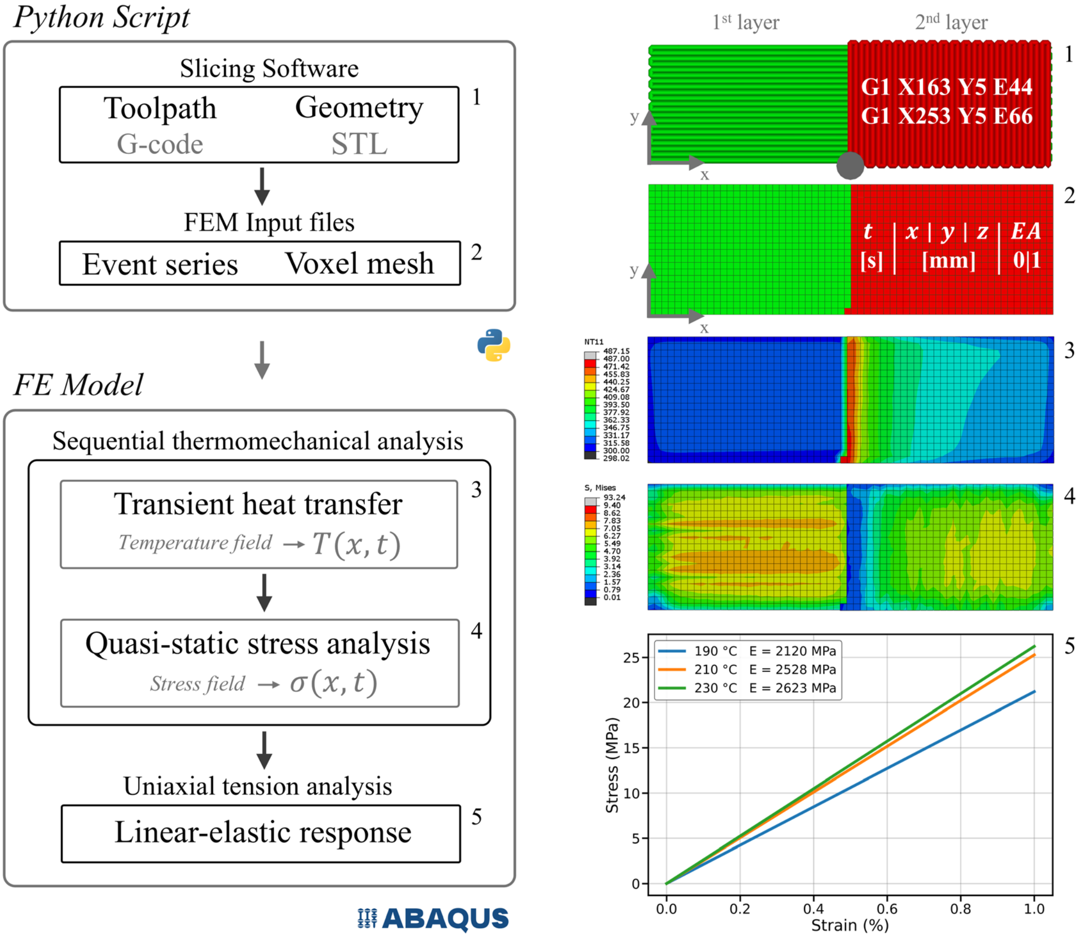

Fig. 1. Model workflow on the right, graphical representation of numerical outputs on the left.

Given that, a motion segment is classified as depositing when extrusion increases beyond a small tolerance:

$$\Delta \mathrm{E} = \mathrm{E}_{i+1} - \mathrm{E}_i > 10^{-6} \tag{1}$$

Retractions, given by negative or zero ΔE, are therefore classified as non-depositing moves. To obtain a time-parameterized trajectory, for each linear move between two points, $\mathbf{p}_i = (x_i, y_i, z_i)$ to $\mathbf{p}_{i+1} = (x_{i+1}, y_{i+1}, z_{i+1})$, is assigned a nominal duration based on the commanded feedrate F. The segment length is

$$L_i = \| \mathbf{p}_{i+1} - \mathbf{p}_i \| = \sqrt{(x_{i+1} - x_i)^2 + (y_{i+1} - y_i)^2 + (z_{i+1} - z_i)^2} \tag{2}$$

and the nominal speed is $v_i = F/60$ mm/s, because in the G-Code, F is expressed in mm/min by default. This ensure that the segment duration $\Delta t_i = L_i/v_i$ and the cumulative process time, obtained by summing Δt_i along the toolpath, are expressed in seconds, consistently with the time base used to drive the event series. The resulting trajectory is finally written as an Abaqus .inp file where each record stores time, nozzle position and one field value representing deposition state:

$$(t_i,\ x_i,\ y_i,\ z_i,\ s_i), \qquad s_i \in \{0,1\} \tag{3}$$

with $s_i = 1$ for depositing segments and $s_i = 0$ for travel segments. In the current implementation, each record is written at the segment start point and segment start time so that the piecewise-linear sequence of records defines the trajectory between consecutive events. In Abaqus, this event series is then used to drive the progressive growth of the active domain: when $s_i = 1$, the deposited region evolves following the nozzle motion, and partial activation can be employed to allow fractional activation of elements intersected by the deposition region.

Process driven voxelization

After generating the event series, a structured cartesian voxel grid is created over the spatial extent of the depositing trajectory. The bounding box is computed using only segments classified as depositing, ensuring the grid encloses the activated volume rather than travel motions. A small margin of approximately half voxel is applied around the bounding box. The voxel dimensions are selected to match the process resolution $\Delta x = \Delta y = w_b$ and $\Delta z = h_\ell$, where w_b is the bead width and h_ℓ is the layer height. Then each voxel (i, j, k) is represented by its center coordinate:

$$\mathbf{c}_{ijk} = (x_0 + (i + \frac{1}{2})\Delta x,\ \ y_0 + (j + \frac{1}{2})\Delta y,\ \ z_0 + (k + \frac{1}{2})\Delta z) \tag{4}$$

The geometry is read as a binary triangulated surface, therefore, the STL is used purely as a geometric mask, defining a volume constraint. For each voxel center $\mathbf{c}_{ijk}$, an odd even ray casting inclusion test is performed where a ray is emitted along the positive x direction and the number of ray triangle intersections is counted. Finally, the voxels whose centers are classified as inside the STL are retained and converted into 8-node hexahedral elements (C3D8). To keep the exported mesh compact, only grid nodes referenced by retained voxels are written. The algorithm first collects all used grid nodes, then assigns contiguous node IDs in a consistent order, sorted by k, j, i, and finally generates contiguous element IDs using the mapped node indices. The resulting mesh is written as an Abaqus .inp file.

Numerical model and governing equations

Consequently, an Abaqus/Standard model is created and the generated voxel mesh is imported, representing the deposition domain where the material is progressively activated and driven by the time-parameterized event series. Let $\Omega(t) \subset \Omega_{\mathrm{mesh}}$ denote the active portion of the voxel mesh at time t. Each event record is mapped to an evolving deposited region; in Abaqus this is implemented through partial activation, allowing fractional activation of intersected elements when required. The same activation strategy is used in both the thermal and the quasi-static analyses, enabling the evaluation of the thermal evolution and its impact on the residual stress field.

Transient thermal formulation

Thermal history during deposition and cooling is computed by solving transient heat conduction over the growing domain $\Omega(t)$. Neglecting internal heat generation, the governing equation reads

$$\rho c_p \frac{\partial T}{\partial t} = \nabla \cdot (k \nabla T) \tag{5}$$

where $T(x, t)$ is the temperature field, k is the thermal conductivity, ρ the density, and c_p the specific heat. Deposition is modelled by prescribing the extrusion temperature as the initial thermal state of newly activated material. Practically, a uniform predefined temperature field is assigned to the part set, including still inactive elements, so that, at the activation time, newly activated elements enter the computation already initialized at the extrusion temperature, while the temperature of previously active material evolves by conduction and boundary heat losses. In fact, heat exchange with the environment is modelled through convection and radiation on exposed surface element at the activation time $\Gamma_{exp}(t)$:

$$-k \nabla T \cdot \mathbf{n} = h\,(T - T_\infty) + \varepsilon \sigma_{SB}(T^4 - T_\infty^4) \tag{6}$$

where h is the film coefficient, T_∞ is ambient temperature, ε is surface emissivity, and σ_{SB} is the Stefan-Boltzmann constant. The interaction with the build plate is represented by a prescribed temperature on the surface in contact with the building plate Γ_{bed}, imposing $T = T_{bed}$ during the deposition step to mimic the building platform maintained at controlled temperature. This constraint is then removed in the cooling step, so that the thermal evolution after deposition is governed by ambient heat losses consistently with Eq. (6). The transient problem is solved using an implicit time integration scheme with a fixed timestep aligned with the event series timeline.

Quasi-static thermoelastic formulation

Residual stresses and distortions are computed in the subsequent quasi-static analysis on the same evolving domain $\Omega(t)$. Neglecting inertia and body forces, mechanical equilibrium is governed by

$$\nabla \cdot \boldsymbol{\sigma} = \mathbf{0} \tag{7}$$

The material response is modelled as isotropic thermoelasticity with temperature-dependent stiffness. The stress tensor is computed as

$$\boldsymbol{\sigma} = \mathbb{C}(T) : (\boldsymbol{\varepsilon} - \boldsymbol{\varepsilon}_{th}) \tag{8}$$

where $\mathbb{C}(T)$ is defined by a temperature-dependent Young's modulus $E(T)$ and a constant Poisson's ratio ν. Thermal strain is assumed to be isotropic and derived from the coefficient of thermal expansion $\alpha(T)$:

$$\boldsymbol{\varepsilon}_{th} = \left(\int_{T_0}^{T} \alpha\,(\theta)\, d\theta \right) \mathbf{I}, \tag{9}$$

with T_0 denoting the reference temperature for zero thermal strain. The temperature history $T(x, t)$ computed in the heat transfer analysis is imported as a time-dependent predefined field and applied over the same deposition and cooling timeline. Building plate adhesion is represented by fixing the displacement field on the base region Γ_{bed}, while the remaining surfaces are free. Geometric nonlinearity is enabled to capture distortion accumulation during cooling. The solution provides the final residual stress field and the distorted configuration at the end of cooling, which are then used as the initial state for the tensile test.

Linear elastic tensile test

At the end of the coupled thermomechanical process simulation, the model provides a distorted configuration and a spatially varying residual stress field $\boldsymbol{\sigma}_{\text{res}}(\mathbf{x})$. This final state is used as the initial condition for a subsequent virtual tensile test aimed at evaluating the elastic response of the printed specimen while accounting for process induced residual stresses.

The tensile simulation is performed as a static analysis under the assumption of linear elastic behavior. The initial stress state is introduced by importing $\boldsymbol{\sigma}_{\text{res}}(\mathbf{x})$ on the final deformed configuration from the thermomechanical solution, so that the tensile response is computed as an incremental perturbation around the cooled, residually stressed state.

During the tensile step, the equilibrium of the incremental problem is enforced:

$$\nabla \cdot \Delta\boldsymbol{\sigma} = \mathbf{0} \tag{10}$$

where $\Delta\boldsymbol{\sigma}$ is the stress increment induced by the applied tensile displacement. The constitutive response is linear elastic:

$$\Delta\boldsymbol{\sigma} = \mathbb{C}\,\Delta\boldsymbol{\varepsilon} \tag{11}$$

with $\mathbb{C}$ defined by Young's modulus E and Poisson's ratio ν. The total stress during the tensile test is then obtained as the superposition of the imported residual field and the tensile increment:

$$\boldsymbol{\sigma}(\mathbf{x}) = \boldsymbol{\sigma}_{\text{res}}(\mathbf{x}) + \Delta\boldsymbol{\sigma}(\mathbf{x}) \tag{12}$$

The tensile test is imposed in displacement control to remain in the linear regime. One grip region is fully constrained while a prescribed axial displacement is applied on the opposite grip with all remaining external surfaces left traction-free. The reaction force F is obtained from the constrained/loading region and used to compute the nominal engineering stress:

$$\sigma_{\text{eng}} = \frac{\text{F}}{\text{A}_0}, \qquad \varepsilon_{\text{eng}} = \frac{\Delta\text{u}}{\text{L}_0} \tag{13}$$

where A_0 is the initial cross-sectional area of the gauge section and L_0 its reference length. The apparent elastic modulus is evaluated from the slope of the σε curve within the prescribed small-strain window.

Application case

ASTMD638 14 Type I

The proposed workflow is verified by manufacturing ASTM D638-14 Type I specimens and characterizing their tensile response according to the same standard [17]. This verification route provides a reproducible geometry and a widely accepted testing framework for plastics, enabling an objective comparison between experimental results and model predictions across different processing conditions. The reference geometry and the discretization adopted in the numerical analysis are shown in Figure 2. As explained in the methodology section the voxel pitch is selected to match the bead resolution employed in the process, ensuring that the simulated activation domain is consistent with the deposition architecture. Specimens were manufactured using an infill-only strategy with 0°/90° alternating rasters between layers and no external perimeters walls, so that the mechanical response is governed solely by the infill structure, an aspect known to strongly affect void formation, interlayer bonding, and the resulting strength in FFF parts [21-23]. Three manufacturing conditions were investigated by varying only the nozzle temperature at 190, 210, 230 °C, while keeping the building plate temperature at 60 °C and the deposition speed constant at 60 mm/s with cooling fans disabled to avoid forced convection effects and better approximate a natural convection dominated cooling condition, consistent with the assumptions implemented in the thermal model. Furthermore, to ensure numerical and experimental alignment, the time step of the model is chosen based on the same deposition kinematics adopted experimentally, so that the activation sequence reproduces the physical deposition timing.

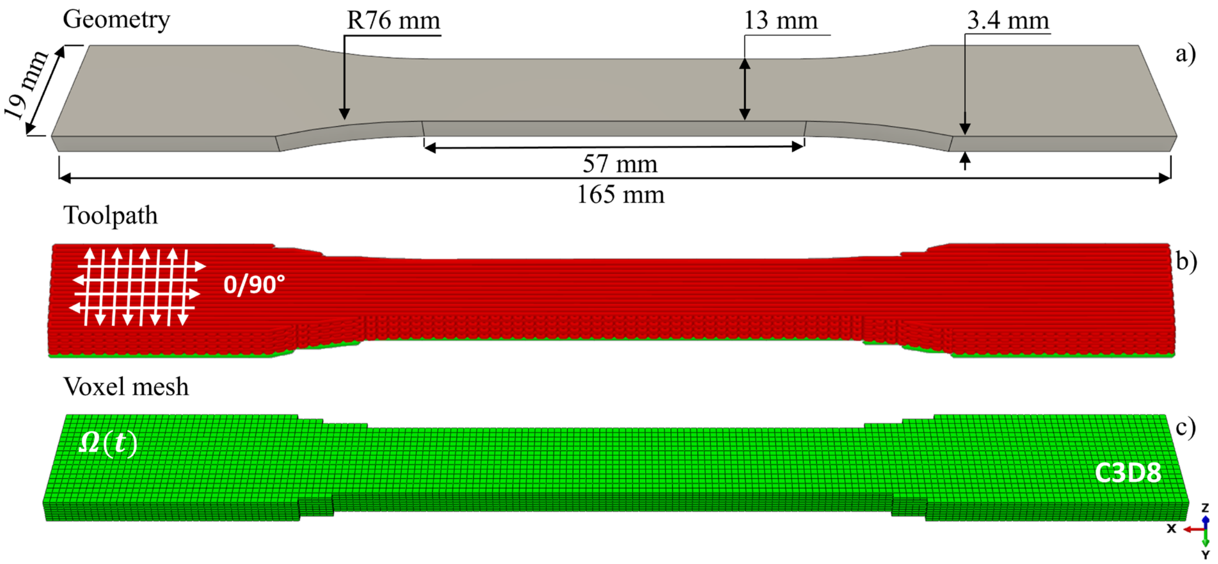

Fig. 2. a) ASTM D638-14 Type I specimen geometry, b) nozzle toolpath and c) voxel mesh.

Commercial PLA Ingeo™ was used to manufacture the specimens. Material properties and thermal boundary parameters adopted in the numerical model are summarized in Table 1. Density and baseline thermo-mechanical properties were taken from NatureWorks datasheets and consolidated literature sources [18-20,24-27]. Thermal conductivity and specific heat were selected consistently with process-oriented thermal models for PLA in material extrusion [25]. Temperature-dependent elastic modulus and coefficient of thermal expansion (CTE) were prescribed via piecewise-linear functions following published dynamic mechanical analysis (DMA) trends for PLA, which report a pronounced modulus drop across T_g and an increasing CTE with temperature [26,27,30]. The machine used is a commercial 3D printer, Anycubic Kobra Max 2, equipped with a 0.8 mm nozzle on the extrusion head. This nozzle allowed to deposit 0.4 mm layer height and 0.96 mm layer width beads, which correspond to the voxel dimensions.

Table 1. PLA properties and thermal boundary parameters adopted in the numerical model. [18-20,25-30]

Table 1a. Constant properties and boundary parameters.

Density	ρ	1240 kg/m³
Thermal conductivity	k	0.13 W/m·K
Specific heat	c_p	1800 J/kg·K
Ambient temperature	T_∞	296.15 K
Emissivity	ε	0.92
Convection coefficient	h	10 W/m²·K
Stefan-Boltzmann constant	σ	5.67037×10^{-8} W/m²·K⁴
Bed temperature	T_{bed}	333.15 K

Table 1b. Temperature dependent E(T) and α(T).

Temperature T (K)	E (MPa)	α (1/K)
293.15	3300	8.0×10^{-5}
323.15	2220	8.0×10^{-5}
343.15	285	1.5×10^{-4}
423.15	80	2.0×10^{-4}
503.15	10	2.0×10^{-4}

Finally, for each nozzle temperature, five specimens were printed to quantify repeatability and scatter. Quasi-static tensile tests were performed on an Instron 4505 universal testing machine following ASTM D638 [17] at room temperature. After printing, specimens were stored under vacuum and released immediately prior to testing to minimize post-processing moisture effects. Specimens were aligned in wedge grips and loaded in displacement control at a crosshead speed of 5 mm/min. Force and crosshead displacement were recorded continuously and converted to engineering stress-strain curves, with engineering stress computed from the initial gauge-section area and engineering strain obtained from the crosshead displacement normalized by the nominal gauge length. The elastic modulus was evaluated consistently for all replicates and temperatures as the slope of the initial linear portion of the engineering stress-strain response.

Results and Discussion

Thermal distribution and process induced deformations

Figure 3 shows the relationship between the temperature field and the process-induced distortions predicted by the sequential thermo-mechanical simulation. The frame is taken right at the end of deposition, at the start of the cooling step. At this moment, the temperature (NT11) still shows clear spatial gradients, mainly related to the regions deposited last. The displacement field (U), instead, already includes the accumulated effect of non-uniform thermal contraction.

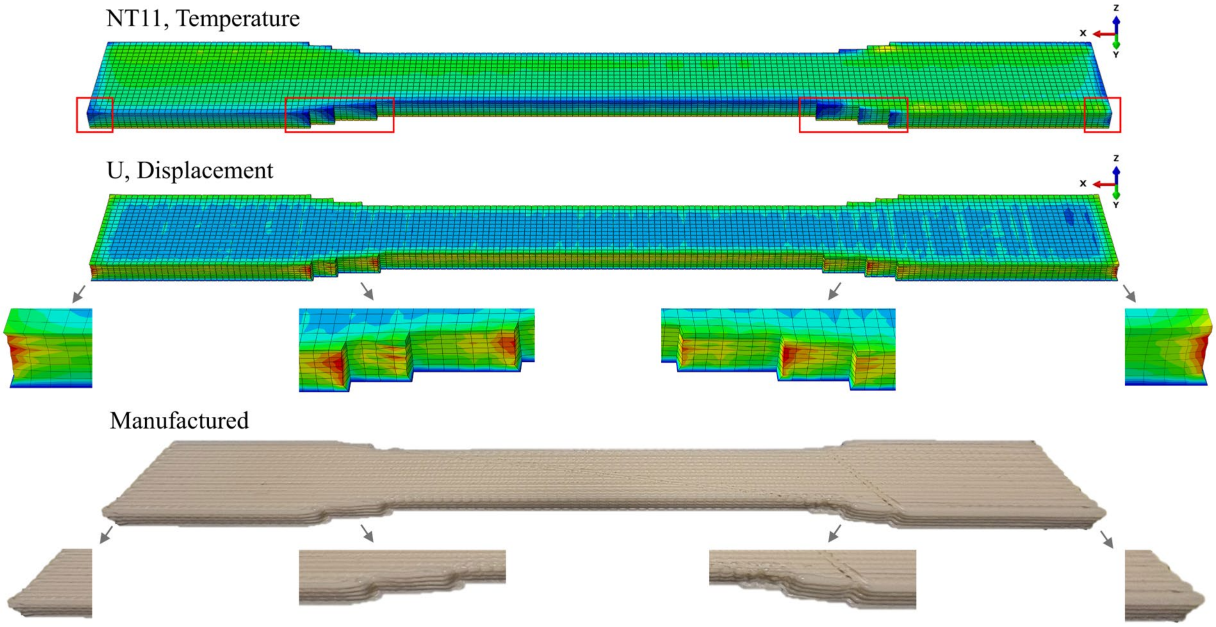

Fig. 3. Process induced deformations during cooling affecting the dimensional accuracy of the manufactured component.

A clear trend can be observed: regions that are cooler at this time, especially near free edges, also tend to show larger local displacements. This is consistent with faster heat loss at exposed boundaries, which promotes differential shrinkage and warpage. The deformation is not uniform along the specimen, it concentrates near geometrical transitions and near the ends, where stiffness changes and boundary effects amplify the response. The zoomed views at the corners highlight this behaviour. Corners appear colder than the central region at the same process time, likely because they have a higher surface to volume ratio and are more exposed to convection and radiation. Even if this interpretation is qualitative at this stage, the same zones also show localized distortion patterns in the displacement contours. These patterns are visible both in the FEM results and on the manufactured specimens. When comparing the three printing temperatures, the overall deformation mode remains similar, but small and consistent differences in displacement magnitude and distribution are observed.

This indicates that the nozzle temperature affects the level of process-induced distortion, even without changing the general trend. Finally, the interaction with the build plate affects the deformation as well. The first layers are partially constrained by the contact with the plate, while the upper regions can deform more freely during cooling. This condition leads to a local thickening near the bottom layers, the so-called “elephant’s foot”, and contributes to the distortion observed after cooling.

Tensile response

Tensile testing on ASTM D638 PLA specimens indicates that the selected extrusion temperature affects the mechanical response, particularly in the initial stiffness, yielding, and the evolution toward failure. The elastic modulus and 0.2% offset yield parameters are reported in Table 2.

Table 2. Elastic properties and 0.2% offset yield parameters, mean ± standard deviation.

Temperature	E [GPa]	$\boldsymbol{\sigma}_{\mathbf{y,0.2\%}}$ [MPa]	$\boldsymbol{\varepsilon}_{\mathbf{y,0.2\%}}$ [%]
190 [°C]	2.66 ± 0.14	32.6 ± 2.0	1.43 ± 0.06
210 [°C]	2.50 ± 0.19	38.7 ± 0.8	1.86 ± 0.05
230 [°C]	2.21 ± 0.20	36.0 ± 2.7	1.96 ± 0.06

A progressive decrease in Young’s modulus is observed with increasing extrusion temperature, from 2.66 ± 0.14 GPa at 190 °C to 2.50 ± 0.19 GPa at 210 °C and 2.21 ± 0.20 GPa at 230 °C. These values are consistent with the expected order of magnitude for PLA, in fact, industrial datasheets for commercially available PLA grades typically report tensile moduli on the order of 2–4 GPa, depending on grade and conditioning [18,19]. Similarly, literature reviews on PLA mechanical behaviour report moduli in the GPa range, with variations driven by crystallinity and thermal history [20]. Therefore, the modulus levels reported in Table 2 seem suitable for comparison across the three processing conditions. With respect to yielding, the 0.2% offset yield stress $\sigma_{y,0.2\%}$ lies in the tens of MPa range, reaching its maximum at 210 °C and decreasing slightly at 230 °C. This non-monotonic trend is reasonable for FFF produced components, because yielding reflects both the effectiveness of load transfer across inter-bead and inter-layer interfaces and changes in the polymer microstructure associated with processing temperature and cooling conditions. The strength and failure-related metrics are reported in Table 3, while the overall stress-strain evolution for the three temperatures is shown in Figure 4.

Table 3. Tensile strength, characteristic strains, and energy to break, mean ± standard deviation.

Temperature	$\boldsymbol{\sigma}_{\mathbf{max}}$/UTS [MPa]	$\boldsymbol{\varepsilon}_{\mathbf{UTS}}$ [%]	$\boldsymbol{\varepsilon}_{\mathbf{break}}$ [%]	$\mathbf{Energy}_{\mathbf{break}}$ [J]
190 [°C]	41.41 ± 0.54	2.35 ± 0.24	2.35 ± 0.49	0.24 ± 0.02
210 [°C]	46.83 ± 1.17	2.81 ± 0.31	2.85 ± 0.36	0.32 ± 0.01
230 [°C]	43.82 ± 1.95	3.06 ± 0.27	3.06 ± 0.29	0.35 ± 0.04

At 190 °C, the specimens exhibit UTS = 41.41 ± 0.54 MPa with characteristic strains close to the failure occurring at approximately 2.35 %, together with a comparatively low energy to break equal to 0.24 ± 0.02 J. At 210 °C, the UTS increases to 46.83 ± 1.17 MPa, while the energy to break rises to 0.32 ± 0.01 J. At 230 °C, the UTS remains high at 43.82 ± 1.95 MPa and both deformation and energy absorption increase further, as also visible by the higher strain reached before fracture in Figure 4, the energy to break increases to 0.35 ± 0.04 J. Overall, the energy to break increases with printing temperature (190 < 210 < 230 °C), indicating an improved ability of the specimens to absorb mechanical energy prior to fracture. Since this energy is reported as the absolute work absorbed by the specimen, it is inherently geometry dependent and is therefore most robustly interpreted here as a relative comparison among the three extrusion temperatures.

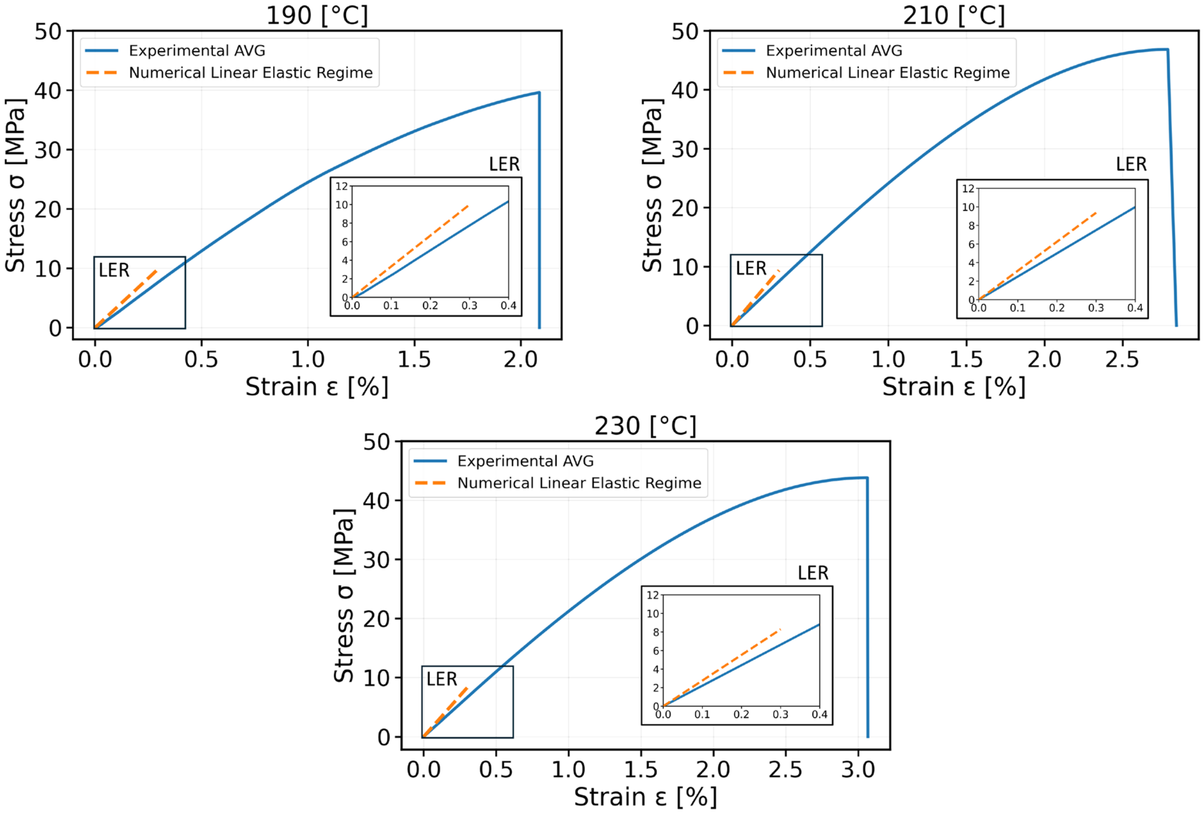

Fig. 4. Mean stress–strain curves for PLA specimens printed at 190, 210, and 230 °C with the highlighted linear-elastic FEM response.

Importantly, the data show that the maximum tensile load-bearing capacity occurs at 210 °C, whereas the lowest UTS is obtained at 190 °C. This observation suggests that 190 °C is likely too low to ensure optimal coalescence and interdiffusion between adjacent filaments, resulting in weaker inter-layer and inter-bead bonding and therefore a higher susceptibility to premature interfacial damage like local debonding and delamination during tensile loading. This interpretation is displayed also on the stress-strain trends in Figure 4, where the 210 °C curve attains the highest peak stress, while the 190 °C curve reaches a lower maximum stress before failure. More generally, increasing nozzle temperature is widely reported to enhance inter-layer and inter-bead welding by increasing melt mobility and promoting polymer chain diffusion and coalescence at interfaces, thereby improving load transfer and reducing the impact of weak interfacial boundaries [21-23]. In this context, the higher peak strength at 210 °C and the increase in energy to break from 190 °C to 230 °C are consistent with progressively more effective interfacial welding as temperature increases, even though the strength maximum occurs at the intermediate temperature 210 °C rather than at the highest temperature investigated. At the same time, the observed decrease in Young’s modulus with increasing temperature suggests that the polymer’s thermal history may also play a role. PLA is known to undergo melt-processing degradation, like chain scission and molecular weight reduction, under sufficiently severe thermal exposure, especially when moisture is present or residence time in the melt is prolonged, which can reduce stiffness and alter the early elastic response [24]. Consequently, the combination of improved failure-related performance, higher energy absorption and high UTS, particularly at 210-230 °C, and reduced elastic stiffness at higher temperatures can be interpreted as a process-dependent trade-off. Higher temperatures improve interfacial welding and damage tolerance while potentially reducing effective stiffness due to thermally driven material changes. Finally, the experimental results were compared with the numerical model results in the linear-elastic regime, where the material was assumed isotropic. For clarity, the FEM prediction is shown only up to $\varepsilon = 0.3\%$ for all temperatures, in order to compare initial stiffness within a common small-strain window. This cutoff is a plotting choice and does not represent a temperature-dependent elastic limit. Within that range, the FEM exhibits a slightly higher initial slope than the experimental mean curves, representing a systematic overestimation of elastic stiffness. This discrepancy is expected because the manufactured specimens with 0/90° infill exhibit anisotropic behaviour and include inter-bead interfaces and residual porosity, which reduce the effective modulus relative to an ideal homogeneous isotropic continuum. Importantly, despite the absolute overestimation, the numerical response remains coherent across the three temperatures, following the same experimental trend of decreasing stiffness from 190 to 230 °C.

Conclusion

This work presented a process-aware, sequential thermomechanical FEM workflow that reproduces material extrusion directly from G-Code by automatically generating a voxel based mesh and a time-parameterized event series for progressive element activation. A transient heat-transfer analysis, where newly activated material is initialized at the extrusion temperature and cooled through convective-radiative exchanges and build-plate boundary conditions, provides the thermal history that drives a subsequent quasi-static thermoelastic analysis to predict residual stresses and distortions after cooling. The simulations highlight how spatial thermal gradients, especially near exposed edges and corners, promote differential shrinkage and warpage, consistent with the observed deformation patterns and build-plate adhesion effects. Experimental tensile tests on PLA ASTM D638 specimens printed at 190-230 °C confirmed a clear process and property relationship: increasing nozzle temperature led to a reduced apparent elastic modulus, while strength and energy absorption generally improved, with maximum UTS observed at 210 °C. The virtual tensile tests captured the same decreasing of stiffness trend, although with a systematic stiffness overestimation attributable to the isotropic continuum assumption and the neglect of porosity and interface effects. Overall, the proposed framework offers a practical route from deposition sequence to mechanical response, supporting process parameter selection. Future developments should incorporate anisotropic constitutive laws based on strand orientation and interfacial features, and extend the mechanical model beyond linear elasticity to account for plasticity and damage, enabling the prediction of yield and failure in a fully process-informed manner.

Acknowledgments

This work was supported by the Ministero dell'Istruzione, dell'Università e della Ricerca, PRIN2022: Recycling of plastic wastes integrating extrusion and additive manufacturing techniques (RELIVE), code 2022FBB37P, CUP: D53D23003520006.

References

[1] ISO, BSEN. "ASTM 52900: 2021." Additive Manufacturing - General Principles - Fundamentals and Vocabulary (2021).

[2] Ahn, Sung-Hoon, et al. “Anisotropic Material Properties of Fused Deposition Modeling ABS.” Rapid Prototyping Journal, vol. 8, no. 4, Oct. 2002, pp. 248–57. DOI.org (Crossref), https://doi.org/10.1108/13552540210441166.

[3] Gao, Xia, et al. “Fused Filament Fabrication of Polymer Materials: A Review of Interlayer Bond.” Additive Manufacturing, vol. 37, Jan. 2021, p. 101658. DOI.org (Crossref), https://doi.org/10.1016/j.addma.2020.101658.

[4] Bellehumeur, Céline, et al. “Modeling of Bond Formation Between Polymer Filaments in the Fused Deposition Modeling Process.” Journal of Manufacturing Processes, vol. 6, no. 2, 2004, pp. 170–78. DOI.org (Crossref), https://doi.org/10.1016/S1526-6125(04)70071-7.

[5] Roy, Mriganka, et al. “Prediction and Experimental Validation of Part Thermal History in the Fused Filament Fabrication Additive Manufacturing Process.” Journal of Manufacturing Science and Engineering, vol. 141, no. 12, Dec. 2019, p. 121001. DOI.org (Crossref), https://doi.org/10.1115/1.4045056.

[6] Trofimov Anton, et al. “Experimentally Validated Modeling of the Temperature Distribution and the Distortion during the Fused Filament Fabrication Process.” Additive Manufacturing, vol. 54, June 2022, p. 102693. DOI.org (Crossref), https://doi.org/10.1016/j.addma.2022.102693.

[7] Frölich, Felix, et al. “An Orientation-Based Homogenization Approach for Predicting Process-Induced Deformations in Extrusion-Based Additive Manufacturing.” Additive Manufacturing, vol. 113, Sept. 2025, p. 105023. DOI.org (Crossref), https://doi.org/10.1016/j.addma.2025.105023.

[8] Esperto, Vitantonio, et al. “Permeability Analysis of Natural and Artificial Fiber Textiles for Liquid Composite Molding Process.” Procedia Manufacturing, vol. 47, 2020, pp. 435–39. DOI.org (Crossref), https://doi.org/10.1016/j.promfg.2020.04.328.

[9] Ramos, Nathalie, et al. “Efficient Simulation of the Heat Transfer in Fused Filament Fabrication.” Journal of Manufacturing Processes, vol. 94, May 2023, pp. 550–63. DOI.org (Crossref), https://doi.org/10.1016/j.jmapro.2023.03.030.

[10] Dassault Systèmes, 3DEXPERIENCE User Assistance, “Event Series.” n.d., https://docs.software.vt.edu/abaqusv2024/English/?show=SIMACAEANLRefMap/simaanl-c-subroutineeventseries.htm. Accessed 13 Dec. 2025.

[11] Esperto, Vitantonio, et al. “Modeling and Simulation of the Robotic Layup of Fibrous Preforms for Liquid Composite Molding.” ESAFORM 2021, Apr. 2021. DOI.org (Crossref), https://doi.org/10.25518/esaform21.475.

[12] G Gambardella, A. “Automated Programming for the Robotic Layup Process.” 2023, pp. 367–74. DOI.org (Crossref), https://doi.org/10.21741/9781644902479-40.

[13] Esperto, Vitantonio, et al. “System Integration for Advanced Manufacturing of Composites by Microwave Preheated Resin Infusion: An Experimental Study.” Journal of Materials Engineering and Performance, vol. 34, no. 10, May 2025, pp. 8759–67. DOI.org (Crossref), https://doi.org/10.1007/s11665-024-10397-7.

[14] Brenken, Bastian, et al. “Development and Validation of Extrusion Deposition Additive Manufacturing Process Simulations.” Additive Manufacturing, vol. 25, Jan. 2019, pp. 218–26. DOI.org (Crossref), https://doi.org/10.1016/j.addma.2018.10.041.

[15] Voříšek, J., and B. Patzák. “GPAMS: A G-Code Processor for Advanced Additive Manufacturing Simulations.” Additive Manufacturing, vol. 65, Mar. 2023, p. 103279. DOI.org (Crossref), https://doi.org/10.1016/j.addma.2022.103279.

[16] Rivet, Iván, et al. “Mechanical Analysis and Optimized Performance of G-Code Driven Material Extrusion Components.” Additive Manufacturing, vol. 61, Jan. 2023, p. 103348. DOI.org (Crossref), https://doi.org/10.1016/j.addma.2022.103348.

[17] ASTM International. ASTM D638-22: Standard Test Method for Tensile Properties of Plastics. 2022.

[18] NatureWorks LLC. Ingeo Biopolymer 3D850 Technical Data Sheet. NatureWorks LLC, n.d., https://www.natureworksllc.com/~/media/Files/NatureWorks/Technical-Documents/Technical-Data-Sheets/TechnicalDataSheet_3D850_monofilament_pdf.pdf. Accessed 7 Dec. 2025.

[19] NatureWorks LLC. Ingeo Biopolymer 3D870 Technical Data Sheet. NatureWorks LLC, n.d., https://www.natureworksllc.com/~/media/files/natureworks/technical-documents/technical-data-sheets/technicaldatasheet_3d870_monofilament_pdf.pdf?la=en. Accessed 7 Dec. 2025.

[20] Farah, Shady, et al. “Physical and Mechanical Properties of PLA, and Their Functions in Widespread Applications - A Comprehensive Review.” Advanced Drug Delivery Reviews, vol. 107, Dec. 2016, pp. 367–92. DOI.org (Crossref), https://doi.org/10.1016/j.addr.2016.06.012.

[21] Cojocaru, Vasile, et al. “The Influence of the Process Parameters on the Mechanical Properties of PLA Specimens Produced by Fused Filament Fabrication—A Review.” Polymers, vol. 14, no. 5, Feb. 2022, p. 886. DOI.org (Crossref), https://doi.org/10.3390/polym14050886.

[22] Tao, Yubo, et al. “A Review on Voids of 3D Printed Parts by Fused Filament Fabrication.” Journal of Materials Research and Technology, vol. 15, Nov. 2021, pp. 4860–79. DOI.org (Crossref), https://doi.org/10.1016/j.jmrt.2021.10.108.

[23] Gajjar, Tusharbhai, et al. “Effects of Key Process Parameters on Tensile Properties and Interlayer Bonding Behavior of 3D Printed PLA Using Fused Filament Fabrication.” Progress in Additive Manufacturing, vol. 10, no. 2, Feb. 2025, pp. 1261–80. Springer Link, https://doi.org/10.1007/s40964-024-00704-y.

[24] Velghe, Ineke, et al. “Review on the Degradation of Poly(Lactic Acid) during Melt Processing.” Polymers, vol. 15, no. 9, Apr. 2023, p. 2047. DOI.org (Crossref), https://doi.org/10.3390/polym15092047.

[25] Liparoti, Sara, et al. “Fused Filament Deposition of PLA: The Role of Interlayer Adhesion in the Mechanical Performances.” Polymers, vol. 13, no. 3, Jan. 2021, p. 399. DOI.org (Crossref), https://doi.org/10.3390/polym13030399.

[26] Blanco, Ignazio, et al. “Specific Heat Capacity and Thermal Conductivity Measurements of PLA-Based 3D-Printed Parts with Milled Carbon Fiber Reinforcement.” Entropy, vol. 24, no. 5, May 2022, p. 654. DOI.org (Crossref), https://doi.org/10.3390/e24050654.

[27] Bianchi, Marica, et al. “Evaluation of the Physical and Shape Memory Properties of Fully Biodegradable Poly(Lactic Acid) (PLA)/Poly(Butylene Adipate Terephthalate) (PBAT) Blends.” Polymers, vol. 15, no. 4, Feb. 2023, p. 881. DOI.org (Crossref), https://doi.org/10.3390/polym15040881.

[28] Morgan, Robert, et al. Emissivity Measurements of Additively Manufactured Materials. LA-UR--7-20513, 1341825, 25 Jan. 2017, p. LA-UR--7-20513, 1341825. DOI.org (Crossref), https://doi.org/10.2172/1341825.

[29] Incropera, Frank P., et al., editors. Fundamentals of Heat and Mass Transfer. 6. ed, Wiley, 2007.

[30] Demiryurek, Sifa Gul. “Evaluation of Dynamic Properties in ABS and PLA Thermoplastics across Frequency Ranges.” Scientific Reports, vol. 15, no. 1, Nov. 2025, p. 42629. DOI.org (Crossref), https://doi.org/10.1038/s41598-025-26846-9.